Double Diffusion Encoding for Probing Radiation-Induced Microstructural Changes in a Tumor Model: A Proof-of-Concept Study With Comparison to the Apparent Diffusion Coefficient and Histology

Gaëtan Duchêne, MS,[1*] Jorge Abarca-Quinones, PhD,[1,2] Natacha Feza-Bingi, BS,[1,3] Isabelle Leclercq, MD PhD,[1,2,3] Thierry Duprez, MD,[1,2] and Frank Peeters, PhD[2]

Background: Microstructure analyses are gaining interest in cancer MRI as an alternative to the conventional apparent diffusion coefficient (ADC), of which the determinants remain unclear.
Purpose: To assess the sensitivity of parameters calculated from a double diffusion encoding (DDE) sequence to changes in a tumor's microstructure early after radiotherapy and to compare them with ADC and histology.
Study Type: Cohort study on experimental tumors.
Animal Model: Sixteen WAG/Rij rats grafted with one rhabdomyosarcoma fragment in each thigh. Thirty-one were imaged at days 1 and 4, of which 17 tumors received a 20 Gy radiation dose after the first imagery.
Field Strength/Sequence: 3T. Diffusion-weighted imaging, DDE with flow compensated, and noncompensated measurements.
Assessments: 1) To compare, after irradiation, DDE-derived parameters (intracellular fraction, cell size, and cell density) to their histological counterparts (fraction of stained area, minimal Feret diameter, and nuclei count, respectively). 2) To compare percentage changes in DDE-derived parameters and ADC. 3) To evaluate the evolution of DDE-derived parameters describing perfusion.
Statistical Tests: Wilcoxon rank sum test.
Results: 1) Intracellular fraction, cell size, and cell density were respectively lower (−24%, $P < 0.001$), higher (+7.5%, $P < 0.001$) and lower (−38%, $P < 0.001$) in treated tumors as compared to controls. Fraction of stained area, minimal Feret diameter, and nuclei count were respectively lower (−20%, $P < 0.001$), higher (+28%, $P < 0.001$), and lower (−34%, $P < 0.001$) in treated tumors. 2) The magnitude of ADC's percentage change due to irradiation (16.4%) was superior to the one of cell size (8.4%, $P < 0.01$) but inferior to those of intracellular fraction (35.5%, $P < 0.001$) and cell density (42%, $P < 0.001$). 3) After treatment, the magnitude of the vascular fraction's decrease was higher than the increase of flow velocity (33.3%, vs. 13.3%, $P < 0.001$).
Data Conclusion: The DDE sequence allows quantitatively monitoring the effects of radiotherapy on a tumor's microstructure, whereas ADC only reveals global changes.
Evidence Level: 2.
Technical Efficacy: Stage 4.

J. MAGN. RESON. IMAGING 2020;52:941–951.

DIFFUSION MAGNETIC RESONANCE IMAGING (dMRI) is sensitive to the random Brownian motion of water molecules within the tissue microenvironment, thereby reflecting its structure at a voxel scale.[1] The simplest metric giving insight into the tissue's microstructure is the apparent diffusion coefficient (ADC), which features the global free-water diffusivity in a voxel.[1] Since the early 1990s, ADC has been investigated in a wide range of pathologic conditions

View this article online at wileyonlinelibrary.com. DOI: 10.1002/jmri.27119

Received Dec 20, 2019, Accepted for publication Feb 18, 2020.

*Address reprint request to: G.D., Brussels, Belgium. E-mail: gaetan.duchene@uclouvain.be

From the [1]Department of medical imaging, Institut de Recherche Expérimentale et Clinique, Université Catholique de Louvain, Brussels, Belgium; [2]MRI unit, Department of medical imaging, Cliniques Universitaires Saint-Luc, Brussels, Belgium; and [3]Laboratory of Hepato-gastroenterology, Institut de Recherche Expérimentale et Clinique, Université catholique de Louvain, Brussels, Belgium

and is currently routinely used in cancer imaging for both diagnosis and posttreatment follow-up.[2] In tumors, the ADC is usually lower than in healthy tissues, mainly due to their higher cell density, which impedes water mobility. However, correlations between the ADC and the actual cell density have been investigated and appear to be dependent on the tumor type.[3,4] To elucidate the link between diffusion measurements and histological features of tumors, microstructure dMRI has recently emerged as a microstructural technique.[5,6]

The standard diffusion sequence, also referred to as single diffusion encoding (SDE), uses two diffusion encoding gradients separated by a diffusion time Δ. The strength of diffusion weighting is usually expressed with the b-value, but can also be described in terms of the q-value defined by q=: $\gamma G\delta^*$ in mm^{-1}, where G is the gradient strength in mT/m, δ^* is the gradient's effective duration in msec, and γ is the proton's gyromagnetic ratio (42.576 MHz/T). The two are related by: $b = (2\pi q)^2(\Delta - \delta^*/3)$. In double diffusion encoding (DDE), two identical gradient pairs separated by a mixing time (t_m) are used for diffusion encoding.[7] DDE offers two additional degrees of freedom, as t_m and the relative angle ψ between the directions of the two gradient pairs can be varied. When t_m tends to 0, displacements during the two encoding periods become correlated and varying ψ was shown to reveal high sensitivity to pore shape.[8] Although DDE should offer significant microstructural information, its clinical applicability remains difficult, mainly because of its inherently long echo time (TE) resulting in poor signal-to-noise ratios (SNRs) or longer scan times, related to the limited gradient strengths available on many clinical systems.[9] Over the last decade, estimating mean cell sizes has been a recurrent topic in dMRI, mainly in microstructure imaging.[10–13] Cell shrinkage or swelling occurs in many pathological/therapeutical processes involving different cell death pathways,[14] of which pore sizing could therefore act as a biomarker. Pore sizing with DDE has been investigated in a wide variety of tissues,[15–18] but remains challenging on clinical systems.[19]

Besides temperature-induced Brownian motion, flow within the microcirculation may also be a source of incoherent motion and therefore may have an impact on dMRI measurements.[20] Diffusion sequences can be sensitive to blood flowing in microvessels, which can even be used for quantitative assessment of microcirculation.[21] For instance, a DDE sequence using only 0 and 180° relative angles and small b-values has been proposed to characterize the microvascularization of the brain.[22] The reason for using 0 and 180° relative angles is that the former is compensated for ballistic flow to which, in turn, the latter has a maximal sensitivity. The notion of ballistic flow refers to the hypothesis that flowing spins have rectilinear trajectories during Δ, which becomes more realistic as Δ is reduced.

A recent study described a DDE sequence with multiple q-values using only 0 and 180° relative angles implemented on a clinical scanner with a clinically-compliant scan time and gradient strength.[23] The sequence was applied on an animal grafted with two rhabdomyosarcomas. These results suggested that the DDE sequence is sensitive to both restricted diffusion and ballistic flow. It was also able to identify cell size variations between viable and necrotic tissues and could discriminate between normally perfused and ischemic tumor subareas. Irradiation has been shown to impact not only the cell density, but the whole tumor microenvironment.[24] Therefore, estimating biomarkers that are closely related to a tumors' microenvironment using an MR sequence sensitive to both restricted diffusion and ballistic flow could be particularly relevant in radiotherapy.

In this work our main goal was to investigate if radiation-induced microstructural changes in tumors could be detected by the DDE sequence and if microstructure modeling of the data could yield parameters that were consistent with histological resections. Furthermore, we aimed to assess the value of the DDE-related microstructural parameters compared to the standard ADC in monitoring the effect of radiations. As the DDE sequence is also sensitive to ballistic flow, the last purpose of the study was to evaluate how radiotherapy impacts the parameters describing the perfusion in the microstructure model.

Materials and Methods

Theory: Signal Modeling

The key concept of microstructure imaging is to model the dMRI signal *S* as the sum of several signals arising from several compartments within a tissue voxel. For instance, in the VERDICT (Vascular, Extracellular and Restricted Diffusion for Cytometry in Tumors) model, the intracellular compartment is modeled by spins diffusing in impermeable spheres and the extracellular matrix is modeled by spins diffusing freely in a tortuous medium,[6] the former and latter featuring restricted and hindered diffusion, respectively. The third compartment takes the vascularization into account. In the VERDICT implementation for the prostate, it is formed by isotropically distributed sticks (zero radius cylinders) in which a high ADC value reflects the global contribution of diffusion and blood flow.[25]

Nonlinear fitting methods may be employed to estimate microstructural parameters but it involves tedious calculations. To overcome this, the Accelerated Microstructure Imaging via Convex Optimization (AMICO) framework has been proposed to linearize the problem by modeling the signal as:

$$S(g(t)) = \sum_{i=1}^{N_c} E_i(g(t))$$

$$E_i(g(t)) = \sum_{k=1}^{N_i} S_{i,k} E(g(t), P_{i,k}) \quad (1)$$

where N_c is the number of compartments and each compartment is subdivided into N_i terms corresponding to N_i values of a descriptor parameter, $P_{i,k}$, specific to each compartment (eg, the mean cell size). In Eq. ((1), g(t) is the diffusion encoding gradient waveform of

a particular measurement, E is the signal attenuation, and, $S_{i,k}$ is the signal amplitude. The E_i's can therefore be calculated for predefined values of $P_{i,k}$ before the fitting procedure.[26] With a linear least-squares procedure, signal amplitudes can all be estimated, allowing quantifying total contributions (fractions) of each compartment and estimating mean values of $P_{i,k}$ therein. In this study, signals were modeled as previously,23 where more details can be found about the parameter estimation. Briefly, it consists of an AMICO-VERDICT framework[26] adapted for ballistic flow, and made of three compartments:

- An intracellular compartment made of impermeable spheres for which the descriptor parameter P is the radius R_k. Five (N_1 = 5) equidistant radii were used in the interval [5; 20] μm.
- An extracellular compartment of free diffusion with reduced ADC values representing the tortuosity. The descriptor parameter P is the ADC, D_k, for which four (N_2 = 4) equidistant values in [1; 2] μm^2/ms were used.
- A vascular compartment displaying plug flow. The descriptor parameter is the plug flow velocity v_k and was evaluated with four (N_3 = 4) values equidistant in [2; 5]x10^{-4} m/s. This velocity range was such that distances traveled by blood spins during both diffusion encoding periods (Δ = 32 msec) range in [12; 32] μm in the plug flow model. Those distances approximately go up to several cell sizes, which we assume to be a reasonable maximum to observe rectilinear motion trough vessels.

Animal Experiments

All animal experimentations were done according to our Institutional Ethical Board for animal handling and manipulations (project number: 2017/UCL/MD/018). Sixteen male WAG/Rij rats (Charles River, Saint Germain Nuelles, France) aged from 10–11 weeks were grafted with rhabdomyosarcoma fragments of about 1 mm^3 in each thigh, leading to a total of 31 tumors, one tumor having not grown at its grafting site. The model was developed and kindly given to us by the Laboratory of Experimental Radiobiology of the Katholiek Universiteit Leuven[27] (Belgium). During the surgical procedure, animals were anesthetized with a mixture of ketamine (80 mg/Kg) and xylazine (10 mg/Kg). During the whole period of growth, tumors' volumes V were calculated daily using the following formula[28]:

$$V = L_L . \frac{L_s^2}{2} \quad (2)$$

where L_L and L_S are respectively the longest and the shortest axes measured with a caliper. After 10–12 days, tumors reached a volume of 2–4 cm^3 at the first MRI session, which defined day 1 of the experiment. A second MRI session was performed 72 hours later, at day 4. Immediately after the first MRI session, nine rats (17 tumors) received a single 20 Gy dose using an IBL-637 ^{137}Cs irradiator (ORIS, Gif-sur-Yvette, France), while the seven (14 tumors) remaining were not irradiated. Ionizing rays were focused on tumors using a 4-cm-thick lead block covering the entire animal pierced by two holes of 4 cm in diameter. During irradiation and imaging sessions, rats were anesthetized with 1.5% isoflurane flowing at 2 L/min in pure O_2. Induction of anesthesia was performed in an induction chamber with 4% isoflurane at 4 L/min in pure O_2. Eleven of the 16 rats (11 treated, 10 control tumors) were euthanatized after the second imaging session with twice the dose of the ketamine/xylazine mixture. The five remaining rats (six treated and four control tumors) were kept alive 3 more days after the second imaging session to evaluate the response to the radiation therapy and were thereafter euthanatized by the same technique as previously described. For each tumor, the growing time was set as the time constant of the volume's exponential growth and was estimated from the two volumes measured at the two imaging sessions.

Histology

Tumors were excised immediately after euthanasia. After extraction, each tumor was immerged into a 4% formaldehyde buffered solution during at least 4 days. A 3-mm-thick transverse slice was then cut in the central part of the tumors. Slices were automatically embedded in paraffin with a Tissue-Tek VIP (Sakura Finetek Europe, Alphen aan den Rijn, The Netherlands) and sliced into 4-μm-thick slices with a Leica rotary microtome (Leica Biosystems, Wetzlar, Germany). Slides were stained with hematoxylin and eosin (H&E) and finally scanned with a 40× objective in an automatic whole-slide scanner, Leica SCN400.

Five fields of 600 × 330 μm^2 were selected in the upper (near the skin), lower (near the muscle), left, right, and central areas of each tumor. The fields were all taken in viable tissue areas, avoiding those where almost no living cells could be found, such as large regions of ischemic or hemorrhagic necrosis, for instance. All analyses of microscopy slides were done with ImageJ (v. 1.50i, NIH, Bethesda, MD).[29]

Three metrics were evaluated in each field: the fraction of stained area, the minimal Feret diameter, and the nuclei count.

The fraction of stained area is the total number of pixels displaying intensity superior to a fixed threshold due to eosin or hematoxylin staining divided by the total number of pixels in the field. Images were first converted to grayscale. The fraction of stained area was therefore an estimate of the fraction of the intracellular environment.

Twenty-five cells exhibiting clearly delineable contours were manually segmented in each field. For each of those cells the minimal Feret diameter was calculated with the "Measure" tool of ImageJ. The minimal Feret diameter is the smallest Feret diameter over all orientations in the plane. This method was preferred to avoid biased size measurements since the samples often included fusiform cells. The minimal Feret diameter is less sensitive to the orientation of nonspherical structures with respect to the cutting plane.[30]

In the center of each of the five fields, a 263 × 143 μm^2 subfield was taken to count the nuclei. This was simply done by marking all nuclei of the subfield with the "Cell count" tool of ImageJ.

For each tumor, the fraction of stained area, the minimal Feret diameter, and the nuclei count were calculated as the mean over the five fields.

MRI

The DDE sequence used in this study is schematized in Fig. 1. It was implemented on a clinical MR system with a single-shot echo-planar imaging (EPI) readout. More information on the sequence can be found elsewhere.23 For each animal, similar DDE and

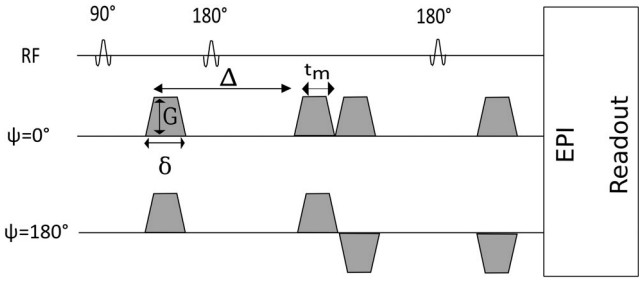

FIGURE 1: Schematic representation of the DDE sequence. Diffusion encoding gradients are represented for 0° and 180° relative angle values that are compensated and not compensated for ballistic flow, respectively. The diffusion time, the mixing time, the gradient duration, and the gradient intensity are represented by Δ, t_m, δ, and G, respectively. Imaging was performed with a single-shot EPI block following a double spin echo pulse sequence and centered on the second spin echo of the 90° excitation pulse.

standard diffusion-weighted imaging (DWI) protocols were performed in the same three orthogonal directions in order to cope with probable anisotropy in tumors. Rats were placed in the 4-channel wrist coil on an Achieva 3T scanner (Philips Healthcare, Best, The Netherlands) equipped with 80 mT/m gradients. Five 4-mm-thick transverse slices were taken and aligned with the two tumors' centers. The in-plane resolution was 2×2 mm^2 with a field of view (FOV) of 130×130 mm^2. EPI and SENSE factors were 33 and 2, respectively.

For the DDE protocol, the following q-values were used: 0, 6.7, 13.3, 20, 26.7, 33.3, and 40 mm^{-1}, corresponding to the following b-values: 0, 100, 390, 890, 1580, 2460, and 3550 s/mm^2, respectively. Sequence timings were δ/Δ = 13/32 msec, echo time / relaxation time (TE/TR) = 108/2000 msec, and t_m = δ = 13 msec. Gradient intensities and slopes were varied, with constant δ, to achieve different q-values and were constrained to maximal values of 80 mT/m and 60 T/m/s, respectively. The applied gradient strength was limited to 53 mT/m along each gradient axis to achieve the maximal amplitude of 80 mT/m. Details about the applied gradient directions can be found elsewhere.23 This emphasizes the potential feasibility of the sequence on a system having (weaker) 53 mT/m gradients. Each nonzero q-value was repeated for ψ = 0 and ψ = 180°, resulting in 13 measurements. Furthermore, each measurement was arithmetically averaged four times (NSA = 4) and four more times with all diffusion gradients having opposed polarities (four measurements with each polarity). The two sets were then geometrically averaged to minimize gradient cross-term artifacts.[31] In total, the DDE acquisition time was 11 minutes 38 seconds, with 13 measurements being done for each of the three orthogonal directions.

For the DWI protocol, 0 and 1000 s/mm^2 b-values were used in the same three orthogonal directions as for DDE. Sequence timings were δ/Δ = 8/27 msec and TE/TR = 55/2000 msec with four signal averages for a total acquisition time of 42 seconds. No phase cycling was used while averaging DDE or DWI data.

Note that the differences in TE and averaging schemes lead to different SNRs between DWI and DDE sequences at b = 0. For a particular sample, a given RF coil, and given that the DDE and DWI sequences have the same EPI readout (same voxel size, bandwidth, etc,), the ratio of SNRs SNR_{DDE}/SNR_{DWI} may be calculated as the signals ratio S_{DDE}/S_{DWI}. A theoretical estimate of this ratio may easily be calculated as $R = S_{DDE}/S_{DWI} = \exp(-TE_{DDE}/T_2)\sqrt{2}/\exp(-TE_{DWI}/T_2)$, where T_2 is the T_2 relaxation time of the sample and the factor $\sqrt{2}$ comes for the doubled number of averages of the DDE sequence. For T_2 ranging between 50 and 100 msec, R would be comprised between 0.5 and 0.83. Experimentally, the signals ratio R ranged between 0.5 and 1in our tumors.

Postprocessing and Data Analysis

All images were denoised with MatLab (R2017a, MathWorks, Natick, MA) software using the algorithm described previously 32 After noise correction, tumor images were registered to their corresponding q = 0 images with a rigid transformation to correct for possible motion or image translation from gradient's dynamic instability. From the 13 DDE's measurements, 13 different $S_{k,i}$ were obtained from Eq. (1) using the "lsqcurvefit" MatLab function, for each of the three orthogonal directions. The following parameters were therefore estimated in each direction and then averaged over the three directions (see [Ref. 23]): the intracellular signal fraction (f_{ic}), the extracellular signal fraction (f_{ec}), the vascular signal fraction (f_{va}), the cell radius (R), the extracellular diffusivity (D), and the plug flow velocity (v). From these parameters, the cell density was calculated as[11]:

$$CD = \frac{f_{ic}}{\frac{4}{3}\pi R^3} \tag{3}$$

Finally, the ADC was calculated for each tumor from the DWI measurements as:

$$ADC = -\frac{\ln(S_{b1000}/S_{b0})}{b_0} \tag{4}$$

where S_{b1000} and S_{b0} are signals for 0 and 1000 s/mm^2 b-values.

Regions of interest (ROIs) enclosing the whole tumor volume were manually delineated on each nondiffusion-weighted (q = 0) DDE image by "G.D." (unexperienced) with consensus of "J.A.Q.," who has more than 30 years of experience in animal experimentation. On these T_2-weighted images, tumor tissues appeared as hyperintense masses located on both rat's thighs. For each tumor, five ROIs corresponding to the five slices were drawn. DDE parameters were therefore calculated for the whole tumor volume. Durations of denoising, registration and AMICO-fitting procedures were respectively 10 seconds, 15 seconds, and 2 seconds on average for one rat (two tumors) with a 3.4 Ghz quad-core processor and 16 GB of RAM.

Tumors were then classified into four groups: 1) controls at day 1; 2) controls at day 4; 3) treated at day 1; and 4) treated at day 4. Sensitivities of MR-derived parameters to radiation-induced changes were evaluated through their percentage change between day 1 and day 4.

Results of histology-derived parameters (fraction of stained area, minimal Feret diameter, nuclei count) and their DDE-derived counterparts (f_{ic}, R, CD) were compared between controls and treated tumors at day 4.

Finally, scatterplots of DDE and histology parameters were drawn to further visualize if measurements of both techniques were consistent. As fields taken on microscopy slides were located only in viable tissue areas, voxels of nonviable tumor areas were excluded when evaluating correlations between MRI and histology parameters. Based on a previous study,[23] a maximal ADC of 1.35 s/µm^2 was heuristically defined as a reasonable criterion to consider a voxel viable. On average, this process led to the exclusion of 7 ± 6% of voxels per tumor.

Statistics

Data are represented as bar plots indicating medians of populations, while error bars indicate distances from the median to the first and third quartiles q_1 and q_3. In the text, data (d) are represented as [d, QD], where QD is the quartile dispersion defined as: QD = $(q_3-q_1)/2$. Significances of differences between medians of two populations were calculated with a Wilcoxon rank sum test in MatLab. In graphs, the significance of results is presented with symbols ***, **, or * to indicate *P*-values inferior to 0.001, 0.01, 0.05, respectively, while the *P*-value was specified for nonsignificant results. In scatterplots, the Spearman correlation coefficient *r* was shown together with the *P*-value of the correlation.

Results

The results showing the efficacy of the radiation therapy are presented in Fig. 2. The growing time evaluated in the whole cohort (31 tumors) between the two imaging sessions was significantly longer for irradiated tumors ([2.7 days, 0.3 days QD] vs. [3.8 days, 0.7 days QD], $P < 0.01$) (see Fig. 2a). From this cohort, five animals (10 tumors) were sacrificed only at day 7 instead of day 4. Their corresponding tumor volumes are represented at the two sessions and at day 7 in Fig. 2b.

Illustrative parametric maps of a control and of an irradiated rat are displayed in Fig. 3.

Parameters estimated in the cohort from DDE and DWI acquisitions are shown in Fig. 4. At day 4 and compared to control tumors, f_{ic} was significantly smaller in treated tumors ([0.21, 0.03 QD] vs. [0.17, 0.02 QD], ie, –24%, $P < 0.001$), R was significantly larger in treated tumors ([10.7 µm, 0.2 µm QD] vs. [11.5 µm, 0.2 µm QD], ie, +7.5%, $P < 0.001$) and CD was significantly smaller in treated tumors ([5.2 10^{-5}/m^3, 0.6 10^{-5}/m^3 QD] vs. [3.2 10^{-5}/m^3, 0.5 10^{-5}/m^3 QD], ie, –38%, $P < 0.001$) (see Fig. 4a).

From Fig. 4b, the magnitude of ADC's percent change in treated tumors ([16.4%, 2.9% QD]) was significantly superior to those of R ([8.41%, 4.5% QD], $P < 0.01$) and D ([9.6%, 4.2% QD], $P < 0.001$). It was inferior to those of f_{ic} ([35.5%, 6.9% QD], $P < 0.001$), f_{va} ([33.3%, 8.9% QD], $P < 0.001$), and CD ([42.1%, 7.6% QD], $P < 0.001$) and was not significantly different from those of f_{ec} ([15.1%, 4.2% QD], $p = 0.76$) and v ([13.3%, 6.4% QD], $p = 0.27$). Finally, the relative decrease of f_{va} in treated tumors was more important than the relative increase in v ([33.3%, 8.9% QD] vs. [13.3%, 6.4% QD], $P < 0.001$).

Histology-derived parameters were quantified from the H&E-stained micrographs and are presented in Fig. 5. Compared to controls, the fraction of stained area was significantly smaller in treated tumors ([48.1%, 1.0% QD] vs. [38.5%, 2.3% QD], ie, –20%, $P < 0.001$), Minimal Feret diameter was significantly larger in treated tumors ([9.9 µm, 0.3 µm QD] vs. [12.7 µm, 0.4 µm QD], ie, +28%, $P < 0.001$) and the nuclei count was significantly smaller in treated tumors ([121, 1.8 QD] vs. [79.9, 1.5 QD], ie, –34%, $P < 0.001$). These outcomes were in line with those of f_{ic}, R, and CD presented earlier (in Fig. 4).

Scatterplots between DDE, DWI, and histological estimates of parameters describing the intracellular compartment

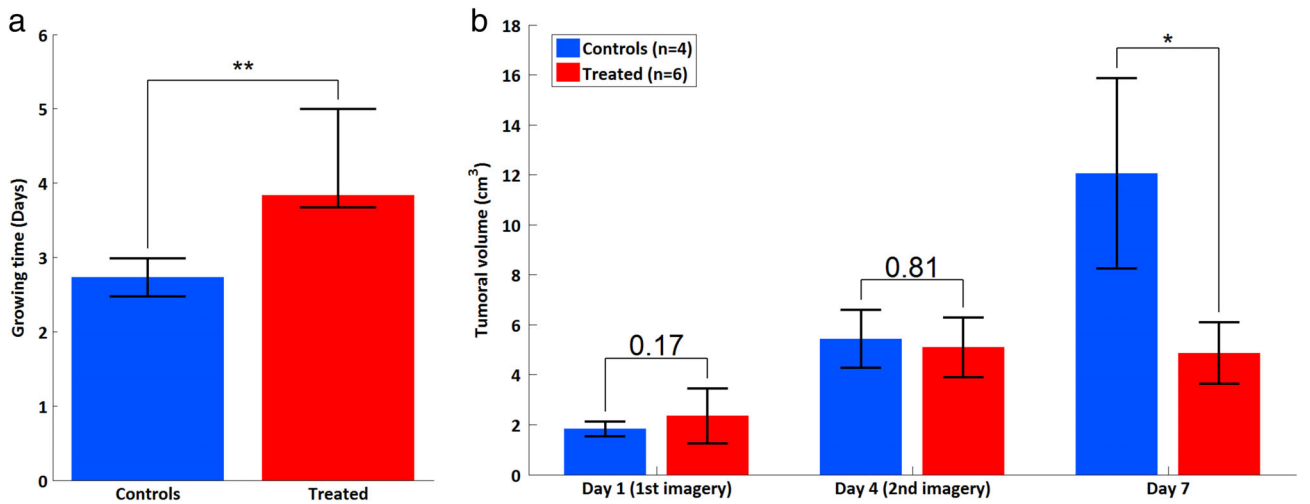

FIGURE 2: Efficacy of the radiotherapy protocol evaluated by tumor growth measurements. In (a), exponential time constants estimated between the two imaging sessions are represented for the whole cohort (*n* = 31 tumors). In (b), tumoral volumes are presented in a limited cohort (*n* = 10 tumors) that was sacrificed 3 days after the second session.

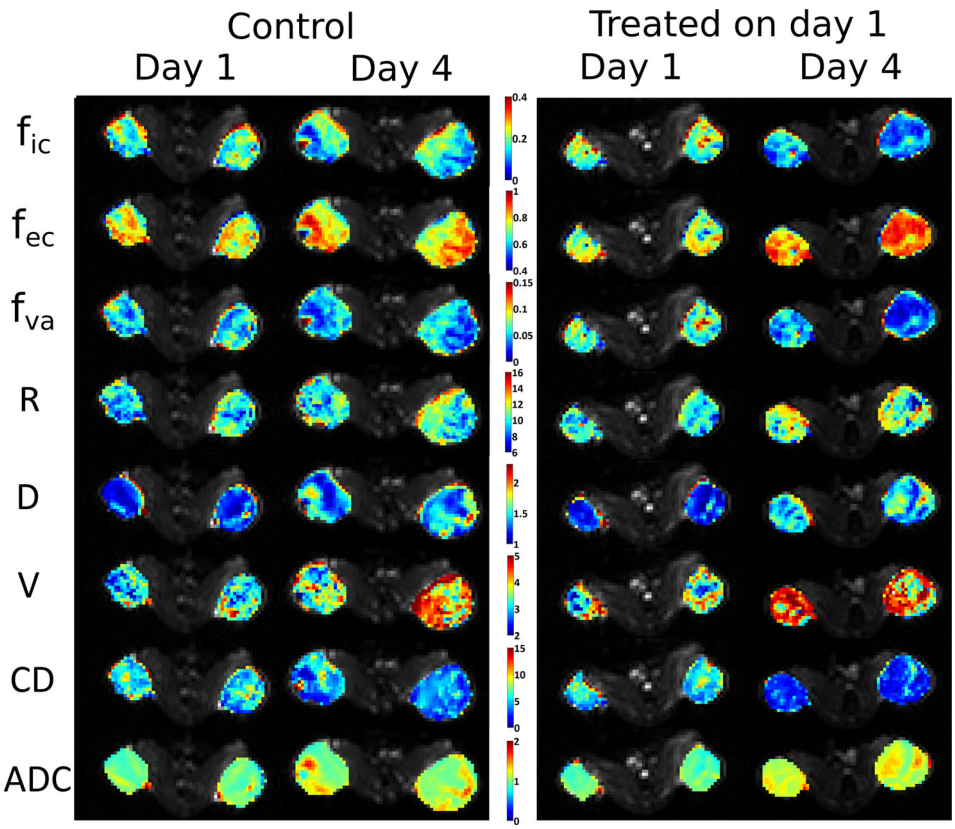

FIGURE 3: Illustration of parametric maps calculated from DDE and DWI data in a control and a treated rat. Fractions are unitless, R is expressed in µm, D and ADC in µm^2/ms, V in ×100 µm/s, and CD in ×10^{-5}/µm^3.

are shown in Fig. 6. High correlation was observed between the intracellular fraction and the fraction of stained area (r = 0.70, P < 0.01). The mean radius vs. the minimal Feret diameter (r = 0.79, P < 0.01), the cell density vs. the nuclei count (r = 0.71, P < 0.01), and the ADC vs. the nuclei count (r = −0.79, P < 0.01) displayed high correlation coefficients as well. However, in these latter scatterplots, data seemed more clustered in two groups corresponding to control and treated tumors, reflecting rather the agreement between the two methods for differentiating the two groups than the actual relationship between MR and histology-derived parameters. Magnitudes of correlation coefficients were comparable between the four comparisons.

Discussion

Irradiation had an impact on the microstructure, which was reflected by a significant increase in growing times observed within 3 days after radiotherapy. Microstructural changes occurring in treated tumors were clearly reflected in the evolution of DDE-derived parameters. These outcomes indicated, among others, decreased intracellular fractions and cell densities but increased cell sizes, which was confirmed by histology. When evaluating the sensitivity of DDE's microstructural parameters through their percentage change following treatment, no particular advantage was found over the standard ADC. Depending on their nature, some microstructure parameters showed higher, lower, or comparable magnitude of percentage change. Analyses of scatterplots showed comparable agreement with histological data for ADC and DDE parameters. Finally, parameters describing the perfusion showed an evolution that would be, in our microstructure model, interpreted as a decreased blood flow but with an increased mean velocity.

Cell swelling is a common feature in radiation-induced cell necrosis and mitotic catastrophe, which are some of the possible cell death pathways for tumor cells undergoing radiotherapy.[14] Note that both an increase in mean cell size and a decrease in intracellular fraction tend synergistically to lower the cell density calculated by DDE, which can explain the strong percentage changes observed in irradiated tumors. On the other hand, the ADC has been shown to decrease with cell swelling but increase with decreasing intracellular fraction.[33] This could explain why variations in cell densities between treated and nontreated tumors were more than twice higher than those of the ADC. Clearly, the ability of a biomarker to reveal a histological process depends on the degree to which the biomarker is exclusively influenced by this process. The ADC has long been recognized as a powerful biomarker of treatment response in tumors,[34] with an inverse relationship between the ADC and the cellularity as a common a priori postulate. In case of efficient treatment, cyto-

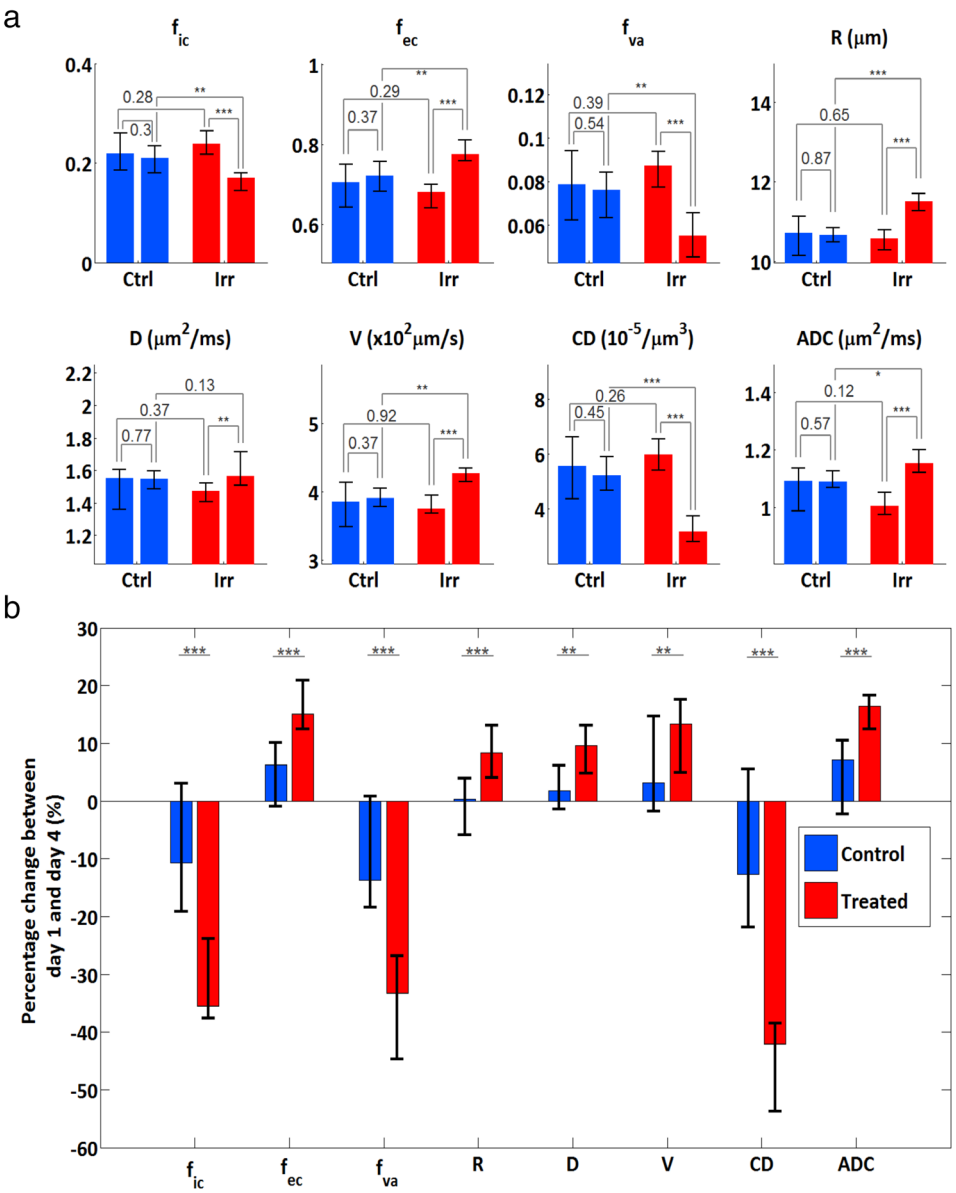

FIGURE 4: Parameters estimated from DDE and DWI sequences. In (a), parameters' values are shown for control and irradiated tumors at day 1 (left bars) and day 4 (right bars). In (b), percentage changes of individual tumors between day 1 and 4 are presented for control and treated tumors.

reduction is reflected by increased free water mobility and subsequently an increase in the ADC value. Although highly influenced by cellularity, several confounding factors have been shown to decrease the ADC even in the case of efficient therapy, such as cell swelling, blood flow reduction, and fibrosis.[35] In this frame, the added value of estimating several microstructural parameters with a simple biophysical interpretation (instead of a single global metric) is rather to discriminate between different processes than to gaining more sensibility of detection.

Signal attenuation arising from the vascular compartment comes from the incoherent motion of blood flowing through microvessels and is therefore tightly linked to the perfusion of the tissues. Quantification of perfusion parameters in tumors can be achieved in vivo with contrast agent bolus tracking modalities such as dynamic contrast-enhanced (DCE)-MRI.[36] The team that provided us with the rhabdomyosarcoma model had already investigated its changes in perfusion parameters after irradiation with DCE-MRI.[37] They showed that the peak and initial slope of the concentration curve were both reduced from 2 days to at least 10 days after receiving a single dose of 8 Gy or a fractionated dose of 15 Gy.[37] In our protocol, a single radiation dose of 20 Gy was delivered and microstructural changes were recorded after 72 hours. Changes in perfusion parameters reported previously37 are therefore very likely to occur in our tumors, which are the same. These results are in line with those of a study investigating the evolution of the time course

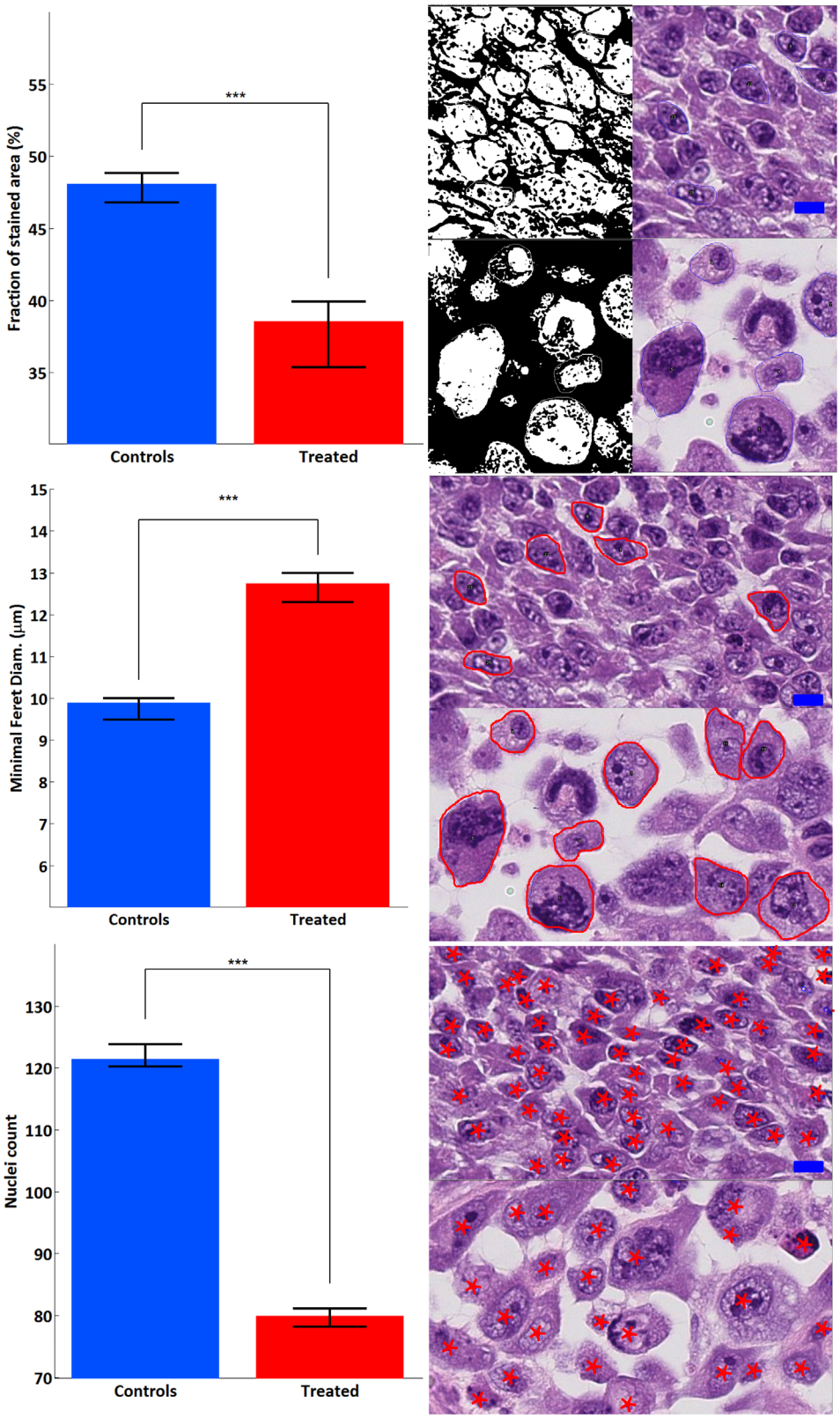

FIGURE 5: Fraction of stained area, minimal Feret diameter, and nuclei count per surface unit estimated from H&E-stained micrographs. On the left panel, bar graphs show differences between control and irradiated tumors. The right panel illustrates binary images after thresholding, manual cell segmentations, and nuclei counting in a control tumor (top) and in an irradiated (bottom) one. Blue horizontal bars represent 10 microns.

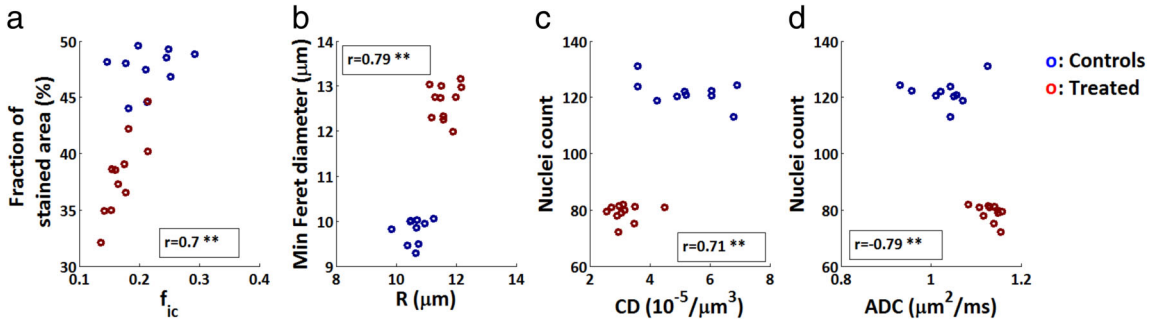

FIGURE 6: Correlations between MRI and histological estimates. Scatterplots of stained area vs. f_{ic}, minimal Feret diameter vs. the mean cell radius, nuclei count vs. CD, and nuclei count vs. ADC are represented in (a–d), respectively. Spearman correlation coefficients *r* and the significance are indicated in each plot.

of tumor perfusion following a single 10 Gy radiation dose.[38] Therein, the authors pointed out that a transient elevation of perfusion due to a drop in interstitial pressure can be observed in the very early phase after radiotherapy, but was rapidly followed by a decrease due to damage to capillaries, thrombosis, and edema.[38] In DCE-MRI, the initial slope and peak of the concentration curve are mainly influenced by the perfusion and may be related to the blood flow and functional capillary volume.[39] Those two parameters were reduced previously.[37] We think that the reduction of the vascular fraction observed in our treated cohort is related to a decrease in functional capillary volume. Blood flow is proportional to the product of the vascular fraction and the mean flow velocity. The former was proportionally more reduced than the latter was increased. Therefore, we interpret this as a global decrease in the blood flow, consistent with the outcomes observed in Ref. 37.

Limitations

Our study has some limitations. First, it assessed the ability of the DDE sequence to detect cell size variations rather than its accuracy in calculating the actual mean cell radius. Indeed, the mean cell diameter was compared to the minimal Feret diameter on histological specimens, which is by design always smaller than the mean diameter. However, it was a more robust method to detect changes in cell size in 2D micrographs, as many fusiform cells were present in our tumor model. Second, the estimate of the cell size may depend on the actual cell structure including different components like organelles, nuclei, etc. In particular, membrane permeability may bias size estimates depending on the diffusion time. Third, the plug flow we used to model the tissue perfusion is clearly an oversimplification of the true blood flow. Subsequently, the precise meaning of the mean plug flow velocity estimated by our DDE sequence remains uncertain and would require further investigation. Plug flow was the simplest model to take this ballistic flow into account and, at least, to evaluate its influence on the total signal. Note that in a previous study on the topic, excellent correspondence was found between large ischemic necrotic areas of the tumors and the vascular fraction map.[23] Moreover, that study demonstrated the presence of ballistic flow in this model and protocol.[23] Fourth, the hypothesis of a purely ballistic flow in capillaries becomes true only when the diffusion time tends to zero. Conversely, Δ must be sufficiently long to keep sensitivity to the intracellular restricted diffusion. A contribution of pseudodiffusion within the vascular compartment is therefore unavoidable. A more refined model should take the ballistic and pseudodiffusion regimes into account for the vascular compartment. Fifth, the DDE sequence implementation could be further improved with phase cycling to correct for pulse imperfections and internal gradient fields. Note that DDE can also be implemented with only one 180° pulse between the two gradient pairs, but at the price of an increased mixing time, which would decrease the sensitivity to pore restrictions.[8,23] Sixth, the performance of DDE-derived parameters were compared to those of the ADC, which remains the most popular metric used in clinical dMRI. Our goal was to give insight into the potential improvements that microstructure imaging with DDE could bring into oncology imaging. However, DDE is not the only advanced diffusion framework and a formal comparison of its performance with, for instance, multiple-b SDE could be done with acquisitions that have at least the same number of measurements. Of course, as a general rule, the more parameters estimated, the more data are needed. Furthermore, DDE sequences generally have lower SNRs than a standard DWI acquisition (second spin echo, thus longer TE, etc.), have a much longer scan time (more than 15 times longer in this study) and numerical procedures to fit microstructure parameters may be highly sensitive to noise (see previous simulations,[23] for instance). Conversely, the ADC is straightforward to estimate from DWI data, which makes it a robust, precise, and easy metric to estimate in a routine protocol. Last, additional studies featuring more tumors could strengthen the conclusion that DDE microstructure parameters feature histopathological evolutions that would be indiscernible with the standard ADC. An increased statistical

power could allow detecting subtle changes in control groups, like necrosis progression, for instance. Furthermore, designing a study with more subgroups receiving different dose levels and monitored at several timepoints would be beneficial.

Conclusion

We used a multiple-q DDE sequence with flow compensated and noncompensated measurements for probing the tumor's microstructure on a clinical scanner. Its sensitivity to changes in cell size was demonstrated on irradiated tumors and the related cell swelling was histologically validated. Furthermore, intracellular fraction and cell density were also in line with histological analyses. Without showing obviously increased sensitivity to treatment-induced microstructural changes as compared to the conventional ADC, DDE parameters allowed us to distinguish between different mechanisms contributing to changes in ADC values. And last, the vascular fraction could be proposed as a biomarker of the actual tumor perfusion. However, further studies focusing on tumor perfusion are mandatory to elucidate what flow characteristics may be retrieved with this kind of diffusion sequence.

References

1. Le Bihan D, Turner R, Douek P, Patronas N. Diffusion MR imaging: Clinical applications. Am J Roentgenol 1992;159(3):591-599.
2. White NS, McDonald C, Farid N, et al. Diffusion-weighted imaging in cancer: Physical foundations and applications of restriction Spectrum imaging. Cancer Res 2014;74(17):4638-4652.
3. Surov A, Meyer HJ, Wienke A. Correlation between apparent diffusion coefficient (ADC) and cellularity is different in several tumors: A meta-analysis. Oncotarget 2017;8(35):59492-59499.
4. Surov A, Hamerla G, Meyer HJ, Winter K, Schob S, Fiedler E. Whole lesion histogram analysis of meningiomas derived from ADC values. Correlation with several cellularity parameters, proliferation index KI 67, nucleic content, and membrane permeability. Magn Reson Imaging 2018;51:158-162.
5. Alexander DC, Dyrby TB, Nilsson M, Zhang H. Imaging brain microstructure with diffusion MRI: Practicality and applications. NMR Biomed 2019;32(4):e3841.
6. Panagiotaki E, Walker-Samuel S, Siow B, et al. Noninvasive quantification of solid tumor microstructure using VERDICT MRI. Cancer Res 2014;74(7):1902-1912.
7. Shemesh N, Ozarslan E, Komlosh ME, Basser PJ, Cohen Y. From single-pulsed field gradient to double-pulsed field gradient MR: Gleaning new microstructural information and developing new forms of contrast in MRI. NMR Biomed 2010;23(7):757-780.
8. Ozarslan E. Compartment shape anisotropy (CSA) revealed by double pulsed field gradient MR. J Magn Reson 2009;199(1):56-67.
9. Yang G, Tian Q, Leuze C, Wintermark M, McNab JA. Double diffusion encoding MRI for the clinic. Magn Reson Med 2018;80(2):507-520.
10. Martin M. Measuring restriction sizes using diffusion weighted magnetic resonance imaging: A review. Magn Reson Insights 2013;6:59-64.
11. Jiang X, Li H, Xie J, et al. In vivo imaging of cancer cell size and cellularity using temporal diffusion spectroscopy. Magn Reson Med 2017;78(1):156-164.
12. Reynaud O. Time-dependent diffusion MRI in cancer: Tissue modeling and applications. Front Phys 2017;5. http://doi.org/10.3389/fphy.2017.00058
13. Ianus A, Shemesh N, Alexander DC, Drobnjak I. Double oscillating diffusion encoding and sensitivity to microscopic anisotropy. Magn Reson Med 2017;78(2):550-564.
14. Lauber K, Ernst A, Orth M, Herrmann M, Belka C. Dying cell clearance and its impact on the outcome of tumor radiotherapy. Front Oncol 2012;2:116-116.
15. Benjamini D, Komlosh ME, Holtzclaw LA, Nevo U, Basser PJ. White matter microstructure from nonparametric axon diameter distribution mapping. Neuroimage 2016;135:333-344.
16. Koch MA, Finsterbusch J. Compartment size estimation with double wave vector diffusion-weighted imaging. Magn Reson Med 2008;60(1):90-101.
17. Komlosh ME, Ozarslan E, Lizak MJ, et al. Mapping average axon diameters in porcine spinal cord white matter and rat corpus callosum using d-PFG MRI. Neuroimage 2013;78:210-216.
18. Koch MA, Finsterbusch J. Towards compartment size estimation in vivo based on double wave vector diffusion weighting. NMR Biomed 2011;24(10):1422-1432.
19. Nilsson M, Lasic S, Drobnjak I, Topgaard D, Westin CF. Resolution limit of cylinder diameter estimation by diffusion MRI: The impact of gradient waveform and orientation dispersion. NMR Biomed 2017;30(7). http://doi.org/10.3389/10.1002/nbm.3711
20. Le Bihan D, Breton E, Lallemand D, Grenier P, Cabanis E, Laval-Jeantet M. MR imaging of intravoxel incoherent motions: Application to diffusion and perfusion in neurologic disorders. Radiology 1986;161(2):401-407.
21. Le Bihan D, Breton E, Lallemand D, Aubin ML, Vignaud J, Laval-Jeantet M. Separation of diffusion and perfusion in intravoxel incoherent motion MR imaging. Radiology 1988;168(2):497-505.
22. Ahlgren A, Knutsson L, Wirestam R, et al. Quantification of microcirculatory parameters by joint analysis of flow-compensated and nonflow-compensated intravoxel incoherent motion (IVIM) data. NMR Biomed 2016;29(5):640-649.
23. Duchene G, Abarca-Quinones J, Leclercq I, Duprez T, Peeters F. Insights into tissue microstructure using a double diffusion encoding sequence on a clinical scanner: Validation and application to experimental tumor models. Magn Reson Med 2019;83(4):1263-1276.
24. Arnold KM, Flynn NJ, Raben A, et al. The impact of radiation on the tumor microenvironment: Effect of dose and fractionation schedules. Cancer Growth Metastasis 2018;11:1179064418761639-1179064418761639.
25. Panagiotaki E, Chan RW, Dikaios N, et al. Microstructural characterization of Normal and malignant human prostate tissue with vascular, extracellular, and restricted diffusion for Cytometry in tumours magnetic resonance imaging. Invest Radiol 2015;50(4):218-227.
26. Bonet-Carne E, Johnston E, Daducci A, et al. VERDICT-AMICO: Ultrafast fitting algorithm for noninvasive prostate microstructure characterization. NMR Biomed 2019;32(1):e4019.
27. Landuyt W, Ahmed B, Nuyts S, et al. In vivo antitumor effect of vascular targeting combined with either ionizing radiation or anti-angiogenesis treatment. Int J Radiat Oncol Biol Phys 2001;49(2):443-450.
28. Tomayko MM, Reynolds CP. Determination of subcutaneous tumor size in athymic (nude) mice. Cancer Chemother Pharmacol 1989;24(3):148-154.
29. Schneider C, Rasband W, Eliceiri K. NIH image to ImageJ: 25 years of image analysis. Nat Methods 2012;9(7):671-675.
30. Briguet A, Courdier-Fruh I, Foster M, Meier T, Magyar JP. Histological parameters for the quantitative assessment of muscular dystrophy in the mdx-mouse. Neuromuscul Disord 2004;14(10):675-682.
31. Neeman M, Freyer JP, Sillerud LO. A simple method for obtaining cross-term-free images for diffusion anisotropy studies in NMR microimaging. Magn Reson Med 1991;21(1):138-143.
32. Manjon JV, Coupe P, Concha L, Buades A, Collins DL, Robles M. Diffusion weighted image denoising using overcomplete local PCA. PLoS One 2013;8(9):e73021.

33. Patterson DM, Padhani AR, Collins DJ. Technology insight: Water diffusion MRI–a potential new biomarker of response to cancer therapy. Nat Clin Pract Oncol 2008;5(4):220-233.

34. Galbán CJ, Hoff BA, Chenevert TL, Ross BD. Diffusion MRI in early cancer therapeutic response assessment. NMR Biomed 2017;30(3). http://doi.org/10.1002/nbm.3458

35. Padhani AR, Liu G, Koh DM, et al. Diffusion-weighted magnetic resonance imaging as a cancer biomarker: Consensus and recommendations. Neoplasia 2009;11(2):102-125.

36. Mazaheri Y, Akin O, Hricak H. Dynamic contrast-enhanced magnetic resonance imaging of prostate cancer: A review of current methods and applications. World J Radiol 2017;9(12):416-425.

37. De Keyzer F, Vandecaveye V, Thoeny H, et al. Dynamic contrast-enhanced and diffusion-weighted MRI for early detection of tumoral changes in single-dose and fractionated radiotherapy: Evaluation in a rat rhabdomyosarcoma model. Eur Radiol 2009;19(11):2663-2671.

38. Bussink J, Kaanders JHAM, Rijken PFJW, Raleigh JA, Van der Kogel AJ. Changes in blood perfusion and hypoxia after irradiation of a human squamous cell carcinoma xenograft tumor line. Radiat Res 2000;153(4):398-404.

39. Cuenod CA, Balvay D. Perfusion and vascular permeability: Basic concepts and measurement in DCE-CT and DCE-MRI. Diagn Interv Imaging 2013;94(12):1187-1204.